

Nanoparticle heterojunctions in ZnS/ZnO hybrid nanowires for visible-light-driven photocatalytic hydrogen generation

Wang, Zheng; Cao, Shao-Wen; Loo, Say Chye Joachim; Xue, Can

2013

Wang, Z., Cao, S. W., Loo, S. C. J., & Xue, C. (2013). Nanoparticle heterojunctions in ZnS/ZnO hybrid nanowires for visible-light-driven photocatalytic hydrogen generation. CrystEngComm, 15(28), 5688-5693.

<https://hdl.handle.net/10356/95757>

<https://doi.org/10.1039/C3CE40523K>

© 2013 The Royal Society of Chemistry. This is the author created version of a work that has been peer reviewed and accepted for publication by CrystEngComm, The Royal Society of Chemistry. It incorporates referee's comments but changes resulting from the publishing process, such as copyediting, structural formatting, may not be reflected in this document. The published version is available at: [DOI: <http://dx.doi.org/10.1039/C3CE40523K>].

Downloaded on 13 Mar 2024 16:48:23 SGT

Nanoparticle Heterojunctions in ZnS/ZnO Hybrid Nanowires for Visible-Light-Driven Photocatalytic Hydrogen Generation

Zheng Wang,^a Shao-Wen Cao,^a Say Chye Joachim Loo,^{a*} and Can Xue^{a*}

Received (in XXX, XXX) Xth XXXXXXXXXX 20XX, Accepted Xth XXXXXXXXXX 20XX

DOI: 10.1039/b000000x

We report one-step hydrothermal preparation of ZnS/ZnO hybrid nanowires consisting of well-distributed nanoparticle-heterojunctions that induce high activity for visible-light-driven H₂ evolution even without any noble metal co-catalysts. During the growth process, the nanoparticulated ZnS nanowires formed first, followed by ZnO nanocrystal growth with intercalation inside the ZnS nanowires. This growth mode could result in enriched ZnS-surface-states on the ZnO nanocrystal surfaces, as evidenced by the weakened absorption features and quenched band gap emission of ZnO in the ZnS/ZnO hybrid nanowires. Further studies by varying the ZnS to ZnO ratio in the ZnS/ZnO hybrids also proved that the population of ZnS-surface-states is crucial to the visible-light activity for photocatalytic H₂ evolution. This work provides a meaningful way to develop heterostructured composites as visible-light-active photocatalysts by using wide band gap semiconductors for solar fuels production.

Introduction

Solar-driven hydrogen generation has been recognized as a green and promising way to produce clean energy and solve fossil fuels shortage problem.¹ In the past a few decades, many photocatalysts have been developed for H₂ generation through solar water splitting based on wide band gap semiconductors, such as TiO₂, ZnO and ZnS,² which are only active in the UV region. Researchers have found that the defects or impurities in their crystal structures could create intermediate states that induce considerable visible-light activities.³ However, because the excitations of these intermediate states are usually accompanied by very fast electron-hole recombination, there are very limited practical uses of such visible-light activities for photocatalytic water reduction.

Hetero-nanostructures, in which two semiconductors are integrated into one nanoscale hybrid, are recently receiving more attention because the interfacial charge transfer can effectively improve the charge separation on both semiconductor units by retarding the recombination process of photogenerated electron-hole pairs.⁴⁻⁶ Further, the coupling of two semiconductors might create interfacial states that induce extra visible-light activity and further facilitate the charge transfer across the heterojunctions.⁷ Hence the strategy of creating nano-heterojunctions would uncover new opportunities on utilizing the visible-light activities of UV-active semiconductors from the defect/impurity/interfacial states by promoting charge separation at the interfaces towards highly efficient photocatalytic reactions.

The hybrid nanostructures of ZnO and ZnS would be an ideal model system to explore such opportunities. Both ZnO and ZnS contain only earth-abundant elements, and are theoretically not active in the visible region due to the wide direct band gap ($E_g=3.4$ eV for ZnO and $E_g=3.7$ eV for ZnS). Both materials have been extensively used as UV-active photocatalysts with a high photostability.⁸⁻¹³ It has been widely reported on the construction of a variety of ZnS/ZnO nanocomposites in the forms of nanotubes^{14,15}, nanorods^{15,16}, nanobelts¹⁷⁻¹⁹, nanosheets²⁰, multipods²¹ and quantum dots²² *et al.* Some reported ZnS/ZnO nanocomposites showed visible light activities in dye degradation, which was attributed to interfacial charge transfer. However, few of them have been used for photocatalytic hydrogen generation under visible-light irradiation.

Herein, we fabricate ZnS/ZnO hybrid nanowires consisting of well-distributed nanoparticle-heterojunctions that induce a high activity for visible-light-driven H₂ evolution even without any noble metal co-catalysts. Further studies reveal that the heterojunctions are crucial in creating ZnS-surface-states on ZnO nanoparticle surfaces, which are responsible for the visible-light-driven photocatalytic H₂ evolution.

Experimental

Synthesis of ZnS/ZnO hybrid nanowires

All chemicals used for experiments, including zinc acetate (99.0%), 16-mercaptohexadecanoic acid (MHA, 90%), isopropyl alcohol (IPA, 99.5%), NaOH, and ethanol (99.9%), were purchased from Sigma Aldrich, and used as received without further purification.

In a typical procedure, 30 mL of aqueous solution containing zinc acetate (0.44 g) and NaOH (1.5 g) was mixed with 30 mL of IPA solution of MHA (0.075 g) under stirring. The homogeneous mixture was transferred into a 100 mL Teflon-lined autoclave which was sealed and heated at 180 °C for 10 h, and then the autoclave reactor was allowed to cool down to room temperature. The obtained products were washed with water and ethanol for several times, and dried in vacuum oven. This sample is denoted as ZZ-a. Control samples were also prepared under the same hydrothermal conditions with different zinc acetate or MHA amount.

Characterization

X-ray diffraction (XRD) measurement was conducted on a Shimadzu XRD-6000 X-ray diffractometer using Cu K α source at a scanning rate of 1°/min with the 2θ range from 10 to 80°. UV-vis diffuse reflectance spectra (DRS) were recorded on a Lambda 750 UV/VIS/NIR spectrophotometer (Perkin-Elmer, USA). The field emission scanning electron microscopy (SEM) images and energy dispersive X-ray spectroscopy (EDS) were performed with a JEOL JSM-7600F scanning electron microscope equipped with energy-dispersive X-ray analysis system. Transmission electron microscopy (TEM) images and selected area electron diffraction (SAED) patterns were recorded on a JEOL JEM-2100F transmission electron microscope at an accelerate voltage of 200kV. The photoluminescence (PL) spectra were collected on a spectrofluorophotometer (Shimadzu RF-5301).

Photocatalytic H₂ production

In a typical photocatalytic experiment, the prepared ZnS/ZnO hybrid sample (5 mg) was dispersed in an aqueous solution (20 mL) of Na₂S (0.25 M) and Na₂SO₃ (0.35 M). The suspension was sealed in a quartz flask and purged with argon for 1 h to drive away the residual air. The photocatalytic hydrogen production was initiated by irradiating the suspension with a 300-Watt Xenon lamp (MAX-302, Asahi Spectra, USA) coupled with a UV-cutoff filter ($\lambda > 420$ nm). The gas product was analyzed periodically through a gas chromatography (Agilent 7890A) with thermal conductivity detector (TCD) detector.

Results and Discussion

Structural characterization of the ZnS/ZnO hybrid nanowires

Fig. 1A shows the XRD pattern of the as-synthesized ZnS/ZnO nanocomposite (ZZ-a). All the diffraction peaks can be perfectly indexed to the standard XRD data ZnS (JCPDS no. 80-0020) and ZnO (JCPDS no. 70-2551). The sharp and intense diffraction peaks indicate the high crystallinity of both ZnO and ZnS. No other impurities were observed in the XRD pattern, which confirms that the ZnO and ZnS composites can be easily prepared through the present one-step hydrothermal method.

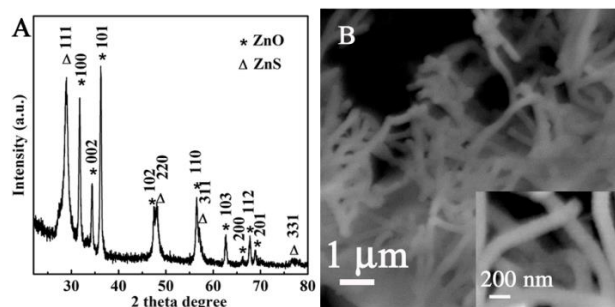


Fig. 1 (A) XRD pattern and (B) SEM image of the as-synthesized ZnS/ZnO nanocomposite (ZZ-a). The inset in (B) is the image at higher magnification.

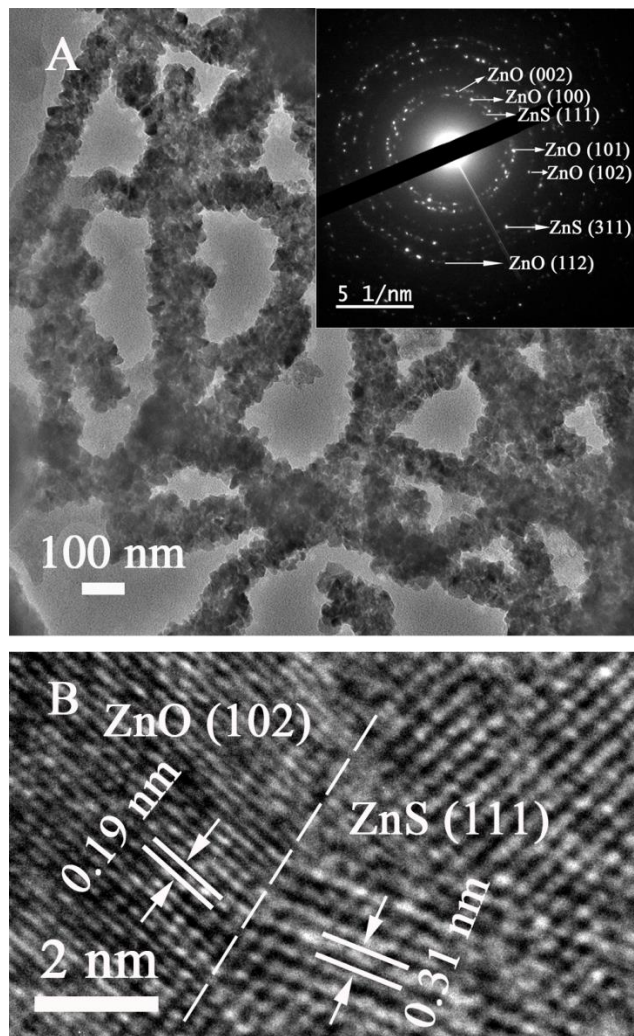


Fig. 2 (A) TEM image of the as-synthesized ZnS/ZnO nanocomposite, the inset shows SAED pattern of image A. (B) HRTEM of ZnS/ZnO interface region in the nanowire.

The SEM image (Fig. 1B) reveals that this ZnS/ZnO composite product is consisted of tangled smooth nanowires with an average diameter of ~100 nm and length up to several micrometers. EDS analysis indicates the relative atomic ratio of S to Zn as 0.57, corresponding to a molar ratio of ZnS to ZnO as 1.33:1, as shown in table 1. Elemental mapping analysis (Fig. S2) suggests the homogeneous distribution of the Zn, S and O element in the composite nanowires. TEM examination (Fig. 2A) of the ZnS/ZnO composite further confirms the nanowire structure which is composed of nanoparticle agglomerates. The SAED pattern (Fig. 2A inset) indicates that these nanowires contain mixed ZnS and ZnO nanocrystals as evidenced by the mixed diffraction features of both components.

Surprisingly, high-resolution TEM (HRTEM) analyses reveal numerous nanoparticle-heterojunctions of ZnS and ZnO. As an example, Fig. 2B shows a ZnS-ZnO junction site, where the left side with an interplanar distance of 0.19nm corresponds to the ZnO (102) plane and the right side with an interplanar distance of 0.31nm corresponds to the ZnS (111) plane. A number of similar ZnS-ZnO heterojunctions can be observed in other HRTEM images as shown in Fig. S3. Moreover, we also observed that one ZnS nanocrystal could form multiple nanoparticle-heterojunctions with other ZnO nanocrystals, and vice versa. These nanoparticle-heterojunctions play important roles on the undermentioned optical properties and photocatalytic performance of the ZnS/ZnO nanocomposites.

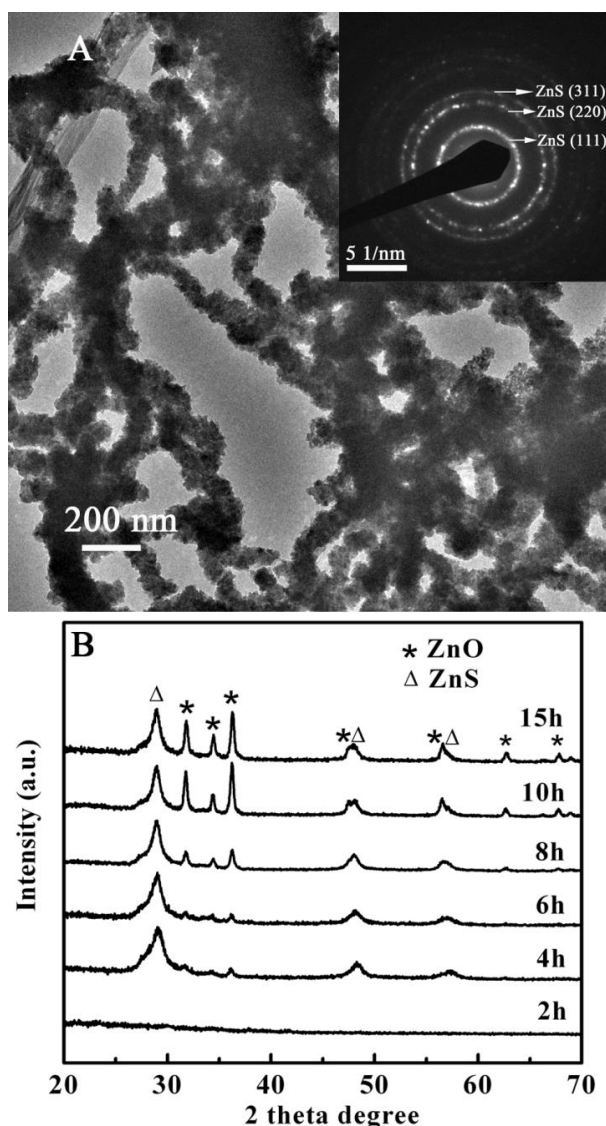


Fig. 3 (A) TEM image of the product after 4 h reaction, the inset shows SAED pattern of image A. (B) XRD patterns of products after different reaction time from 2 h to 15 h.

Growth process of the ZnS/ZnO hybrid nanowires

In order to investigate the growth process of the ZnS/ZnO nanowires, samples with different reaction time varying from 2 h to 15 h were prepared. The XRD patterns (Fig 3B) indicate that ZnS was formed as the major product in the first 4 h reaction, while ZnO is minor. TEM examination (Fig. 3A) confirms the formation of nanoparticulated wires at 4 h reaction. Consistently, the SAED pattern of these nanowires shows only diffraction signatures of ZnS. This result suggests that at the early stage of the reaction, ZnS nanoparticulated wires form first through reaction between zinc acetate and -SH group in MHA.

The XRD signatures of ZnO become more evident after 6 h reaction and it is continue growing up till 10 h. Based on this observation and the TEM analysis of final product, we believe that the ZnO nanocrystals were generated through reaction between Zn^{2+} and the carboxylate group of MHA and inserted within the ZnS nanowire framework. No free ZnO structures were observed. We exclude the direct oxidation of ZnS to ZnO because after the 10 h reaction, the intensity of ZnS peak was not weakened. Prolonging the reaction time to 15 hour did not further increase the intensity of ZnO peaks with respect to the peak of ZnS, and the relative molar ratio of ZnS and ZnO remains no change as compared to that at 10 h reaction (as shown in Table S1). This means that the composition of the ZnS/ZnO hybrid nanowires becomes stable after 10 h reaction.

Photocatalytic H_2 evolution by ZnS/ZnO hybrid nanowires

The prepared ZnS/ZnO hybrid nanowires were used for photocatalytic H_2 generation under visible light ($\lambda > 420 \text{ nm}$) irradiation.

Fig. 4A shows that ZZ-a sample exhibits active visible-light-driven H_2 evolution with a rate of $22 \mu\text{mol}\cdot\text{h}^{-1}\cdot\text{g}^{-1}$. In contrast, no H_2 evolution was observed for commercial ZnS (99.99%, denoted as C-ZnS) and ZnO (99.999%, denoted as C-ZnO) samples due to their large band gap. The stability of the sample was tested over three repeating cycles. Between each cycle of 4 h photocatalytic reaction, the reactor is thoroughly degassed for 1 h. As shown in Fig. 4B, the H_2 evolution rate remains almost no change over the three cycles, indicating that the ZnS/ZnO hybrid nanowires are quite stable during the 12 h photocatalytic reaction.

Comparison samples were prepared by using either 1.5 times higher quantity of zinc acetate (denoted as ZZ-b) or fourfold of MHA (denoted as ZZ-c). XRD patterns (Fig. 4C) indicate that these two samples are also composed of ZnS and ZnO. EDS analyses reveal the molar ratio of ZnS to ZnO as 3:1 for ZZ-c and 1:1.33 for ZZ-b, as shown in table 1. These two samples also show visible-light-driven photocatalytic activity for H_2 evolution at a rate of $7 \mu\text{mol}\cdot\text{h}^{-1}\cdot\text{g}^{-1}$ for ZZ-b and $16 \mu\text{mol}\cdot\text{h}^{-1}\cdot\text{g}^{-1}$ for ZZ-c, respectively.

Table 1 EDS elemental ratio of the ZnS/ZnO nanocomposites with different precursor quantity

Sample	S:Zn Atomic %	ZnS: ZnO molar ratio
ZZ-a	0.57	1.33:1
ZZ-b	0.43	1:1.33
ZZ-c	0.75	3:1

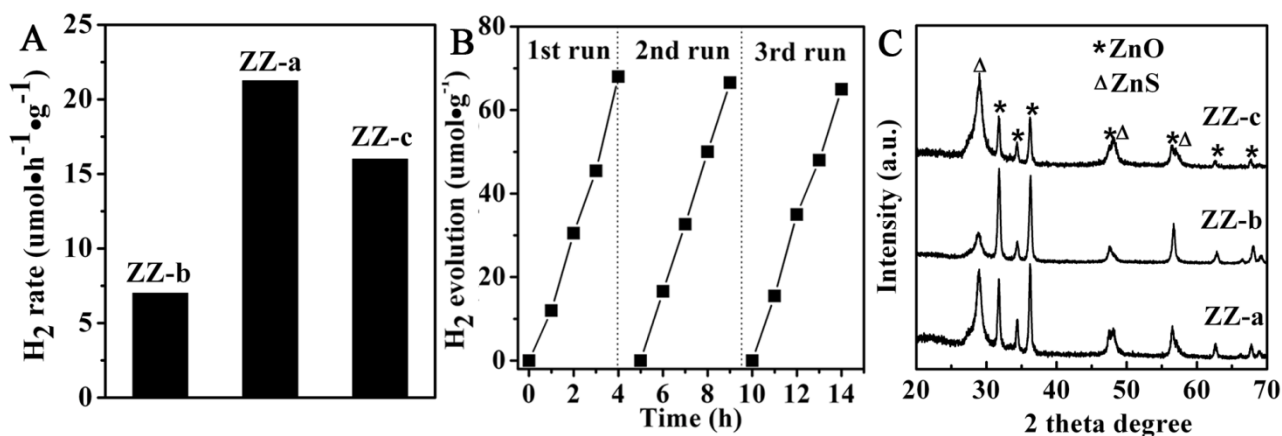


Fig. 4 (A) Comparison of visible light H_2 evolution activities of ZnS/ZnO nanocomposite samples and commercial ZnO and ZnS in mixed aqueous solution of 0.25M Na_2S and 0.35M Na_2SO_3 as sacrificial reagent. Light source: 300W Xenon lamp with an intensity of $120\text{mW}/\text{cm}^2$. (B) Repeating cycles of H_2 evolution in the presence of ZnS/ZnO nanocomposite as photocatalysts under visible light illumination. (C) XRD spectra of three ZnS/ZnO nanocomposite samples with different precursor quantities

Proposed mechanism of visible light activity for H_2 evolution

It is well known that both ZnS and ZnO have large band gap ($>3.2 \text{ eV}$), and thus almost no absorption in the visible light region. However, some recent reports have demonstrated that the ZnS-ZnO nanocomposites may be able to exhibit certain visible-light activities. For example, Hu *et al.* showed that ZnO@ZnS core-shell nanostructures could be used for dye degradation under visible-light irradiation.²³ They proposed that the created ZnS-ZnO interfaces led to a lower band gap energy of the composite than that of individual ZnS and ZnO. According to Schrier's calculation, strained conduction band minimum (CBM) energies are both lowered down for ZnO and ZnS in the ZnO@ZnS core-shell nanowire model so that the overall band gap energy of the ZnO/ZnS heterostructures could be as low as 2.07eV .²⁴

Very recently, Wang *et al.* have analyzed the interface of ZnS/ZnO heterostructures by using scanning transmission X-ray microscopy (STXM) and successfully observed the threshold movement of edge energy across ZnS/ZnO interfaces.²⁵ Although the direction of the threshold shifting on ZnO in Wang's observation is different from Schrier's calculation, both studies still reveal that the band alignment can be shifted at the ZnS/ZnO interface. In addition, Lahiri *et al.* have observed an increase of the work function of ZnO upon the formation of ZnS monolayer on the ZnO surface, which was attributed to band bending and surface dipole moment due to the electronic hybridization of ZnO band structures with the surface states induced by the ZnS

monolayer.⁷ This resulted in an effective band gap of ~2.8 eV, allowing for visible-light excitation.

In our prepared ZnS/ZnO hybrid nanowires, the ZnO nanoparticles formed with intercalation inside the ZnS nanowires. The HRTEM images (Fig. 2 and S3) have proved that almost every ZnO nanoparticle is surrounded by one or more ZnS nanocrystals with directly contacted interfaces. This would create numerous ZnS-surface-states on ZnO nanoparticle surfaces. Thus, as illustrated in Fig. 5, it becomes possible that the electrons at the ZnO-ZnS interfaces could be excited from the banded VB level induced by the ZnS-surface-states to the CB of ZnO for water reduction. By this way, the effective band gap at the interface would be narrowed down, which enables the excitation under visible-light irradiation. The photogenerated holes would be trapped by the ZnS-surface-states and subjected to be quenched by the sacrificial reagent ($\text{S}^{2-}/\text{SO}_3^{2-}$) that facilitates the electron-hole separation.

Effect of ZnS to ZnO ratio

The photocatalytic test results indicate that the ratio of ZnS to ZnO has significant influence on the visible-light activity of the ZnS/ZnO hybrids (Fig. 4A). The ratio of ZnS to ZnO would affect the area of ZnS/ZnO interfaces, and thereby the visible-light absorption as well as photocatalytic activity of the ZnS/ZnO hybrids. This result further demonstrates the essential role of the ZnS/ZnO interfaces on the visible-light-driven H_2 production.

Photoluminescence spectra were measured at the excitation wavelength of 325 nm to study the effect of ZnS to ZnO ratio on

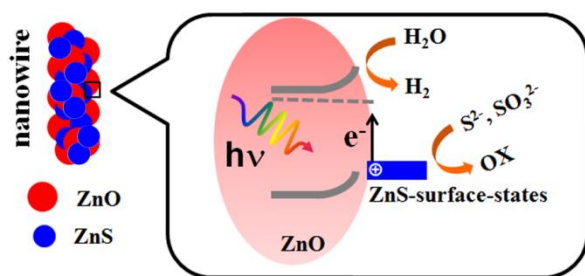


Fig. 5 Proposed mechanism of H_2 evolution over ZnS/ZnO hybrid nanowires under visible light irradiation.

the charge transfer. As shown in Fig. 6A, all the ZnS/ZnO hybrid samples show a UV emission peak at 360 nm, corresponding to the intrinsic band gap emission of ZnS as compared to the commercial ZnS powder.²⁶⁻²⁸ However, the typical band gap emission at 380 nm, as observed for the commercial ZnO powder, was quenched in the ZnS/ZnO hybrids (ZZ-a and ZZ-c). This could be again ascribed to the highly rich ZnS-surface-states on ZnO nanoparticle surfaces, which act as trapping sites and enhance non-radiative recombination of photogenerated charges. For the sample ZZ-b, we observe a red-shifted UV emission band at ~390 nm and broad green emission between 450 nm to 500 nm. It indicates that in this sample with higher ZnO content than ZnS, some ZnO particles may grow larger on the nanowire surfaces instead of being intercalated inside, and are not enriched with ZnS-surface-states. Thus, some intrinsic defects, such as oxygen vacancies and interstitial states, may be present and responsible for the red-shifted near-band-edge emission with a broad tail.^{27,28}

The absorption spectra of the samples also show consistent results. As shown in Fig. 6B, the commercial ZnS shows a typical excitonic absorption peak at 335 nm,²⁹ and the excitonic absorption peak of commercial ZnO is around 357 nm. A simple physical mixture of commercial ZnS and ZnO with 1:1 molar ratio (denoted as Mix) shows a mixed absorption feature of both with an absorption edge below 400 nm. However, our prepared ZnS/ZnO hybrid nanowires showed a broad absorption band at ~400 nm with absorption edge up to 500 nm, which is red-shifted as compared to the absorption feature of commercial ZnO. This observation verifies the formation of afore-proposed ZnS-surface-states on ZnO surfaces, which is responsible for this broad absorption in the visible region.

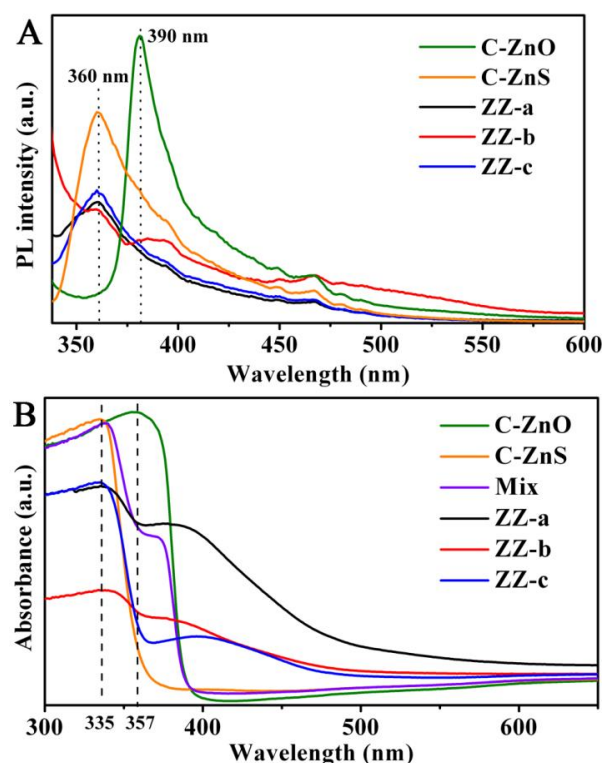


Fig. 6 (A) Photoluminescence and (B) UV-vis absorbance of as-synthesized nanocomposites with different precursor quantities.

Consistently, by comparing ZZ-a with ZZ-c, lower ZnO content results in weaker absorption band near 400 nm since the ZnO-ZnS interfaces are reduced. As such, ZZ-a shows a higher yield of visible-light-driven H_2 evolution than ZZ-c. The sample of ZZ-b exhibits much lower photocatalytic H_2 evolution activity than the other two ZnS/ZnO hybrid samples because the excessive ZnO content led to larger sized ZnO particle outside the nanowire surfaces and relatively less surfaces to form ZnO/ZnS interfaces. In short, these observations suggest that the population of the ZnS-surface-states at the ZnO/ZnS interfaces is directly responsible to the visible-light activity of the ZnS/ZnO hybrid nanowires and thereby their photocatalytic H_2 evolution rate.

Conclusions

In summary, we have fabricated ZnS/ZnO hybrid nanowires consisting of well-distributed nanoparticle-heterojunctions that induce high photocatalytic activity for visible-light-driven H_2 evolution without any noble metal co-catalysts. Further studies suggest that the generated ZnS-ZnO heterojunctions could create ZnS-surface-states on the ZnO nanoparticle surfaces, which induce band bending of ZnO and narrow down the effective band gap at the interface the ZnS/ZnO hybrids, thus allow for visible-light excitation. Variation of ZnS to ZnO ratio in the ZnS/ZnO hybrids also proves that the population of ZnS-surface-states is crucial to the visible-light activity for photocatalytic H_2 evolution. Our studies demonstrate that the UV-active semiconductors can also be used as visible-light photocatalysts for hydrogen production by forming heterojunctions with appropriate interface states. This would provide an alternative way to fabricate composite photocatalysts for solar fuels production.

Acknowledgements

This work was financially supported by NTU Start-Up Grant (SUG), NTU seed funding for Solar Fuels Laboratory, MOE AcRF-Tier1 RG 44/11, MOE AcRF-Tier2 (MOE2012-T2-2-041, ARC 5/13), and CRP (NRF-CRP5-2009-04) from NRF Singapore.

Notes and references

^a Solar Fuels Laboratory, School of Materials Science and Engineering
Nanyang Technological University, 50 Nanyang Avenue, Singapore
639798, Singapore. E-mail: cxue@ntu.edu.sg, joachimloo@ntu.edu.sg

† Electronic Supplementary Information (ESI) available: additional characterization results including XRD, EDS and HRTEM. See DOI: 10.1039/b000000x/

1. N. S. Lewis, *Nature*, 2001, **414**, 589-590.
2. X. B. Chen, S. H. Shen, L. J. Guo and S. S. Mao, *Chem. Rev.*, 2010, **110**, 6503-6570.
3. L.C. Chen, Y.J. Tu, Y.S. Wang, R.S. Kan and C.M. Huang, *J. Photochem. Photobiol., A*, 2008, **199**, 170-178.
4. Z. Shen, G. Chen, Q. Wang, Y. Yu, C. Zhou and Y. Wang, *Nanoscale*, 2012, **4**, 2010-2017.
5. S. W. Cao, J. Fang, M. M. Shahjamali, Z. Wang, Z. Yin, Y. H. Yang, F. Y. C. Boey, J. Barber, S. C. J. Loo and C. Xue, *CrystEngComm*, 2012, **14**, 7229-7235.
6. S. W. Cao, Z. Yin, J. Barber, F. Y. C. Boey, S. C. Loo and C. Xue, *ACS Appl. Mater. Interf.*, 2012, **4**, 418.
7. J. Lahiri and M. Batzill, *J. Phys. Chem. C*, 2008, **112**, 4304-4307.
8. J. Li, S. Ma, X. Liu, Z. Zhou and C. Q. Sun, *Chem. Rev.*, 2012, **112**, 2833-2852.
9. L. Wang, D. Tsan, B. Stoeber and K. Walus, *Adv. Mater.*, 2012, **24**, 3999-4004.
10. X. Wang, G. Liu, Z.-G. Chen, F. Li, L. Wang, G. Q. Lu and H.-M. Cheng, *Chem. Commun.*, 2009, 3452.
11. Y. Hong, J. Zhang, X. Wang, Y. Wang, Z. Lin, J. Yu and F. Huang, *Nanoscale*, 2012, **4**, 2859.
12. S. K. Pahari, A. Sinhamahapatra, N. Sutradhar, H. C. Bajaj and A. B. Panda, *Chem. Commun.*, 2012, **48**, 850-852.
13. Y. Zhang, W. Liu and R. Wang, *Nanoscale*, 2012, **4**, 2394-2399.
14. X. D. Wang, P. X. Gao, J. Li, C. J. Summers and Z. L. Wang, *Adv. Mater.*, 2002, **14**, 1732-1735.
15. X. Huang, M. Wang, M. G. Willinger, L. D. Shao, D. S. Su and X. M. Meng, *ACS Nano*, 2012, **6**, 7333-7339.
16. S. K. Panda, A. Dev and S. Chaudhuri, *J. Phys. Chem. C*, 2007, **111**, 5039-5043.
17. J. Yan, X. S. Fang, L. D. Zhang, Y. Bando, U. K. Gautam, B. Dierre, T. Sekiguchi and D. Golberg, *Nano Lett.*, 2008, **8**, 2794-2799.
18. X. Fan, M.-L. Zhang, I. Shafiq, W.-J. Zhang, C.-S. Lee and S.-T. Lee, *Adv. Mater.*, 2009, **21**, 2393-2396.
19. L. Hu, J. Yan, M. Liao, H. Xiang, X. Gong, L. Zhang and X. Fang, *Adv. Mater.*, 2012, **24**, 2305-2309.
20. L. Nasi, D. Calestani, T. Besagni, P. Ferro, F. Fabbri, F. Licci and R. Mosca, *J. Phys. Chem. C*, 2012, **116**, 6960-6965.
21. P. Chen, L. Gu and X. Cao, *CrystEngComm*, 2010, **12**, 3950-3958.
22. J. Xiao, F. Wang, J. Liu, L. Wang, G. Kai and X. Yu, *Mol. Biosyst.*, 2011, **7**, 2452-2458.
23. Y. Hu, H. Qian, Y. Liu, G. Du, F. Zhang, L. Wang and X. Hu, *CrystEngComm*, 2011, **13**, 3438-3443.
24. J. Schrier, D. O. Demchenko and L. W. Wang, *Nano Lett.*, 2007, **7**, 2377-2382.
25. Z. Wang, J. Wang, T.-K. Sham and S. Yang, *J. Phys. Chem. C*, 2012, **116**, 10375-10381.
26. X. Zhang, M. Chen, J. Wen, L. Wu, H. Gao and D. Zhang, *CrystEngComm*, 2013, **15**, 1908-1913.
27. W.-S. Chae, J.-H. Yoon, H. Yu, D.-J. Jang and Y.-R. Kim, *J. Phys. Chem B*, 2004, **108**, 11509-11513.
28. C.Y. Lan, J. F. Gong, Y. W. Jiang and Q. P. Ding, *CrystEngComm*, 2012, **14**, 8063-8067.
29. S. Wageh, Z. S. Ling and X. Xu, *J. Cryst. Growth*, 2003, **255**, 332-337.

